H_2 production from methanol solution with ca. 100% quantum efficiency by synergy of Cu single atoms and Pt nanodots in a zero-carbon-emission process

Hui Wang,[1] Haifeng Qi,[2] Xiao Sun,[3] Shuya Jia,[4] Xiyi Li,[1] Tina Miao,[1] Lunqiao Xiong,[1] Shihao Wang,[5] Xiaolei Zhang,[4] Xiaoyan Liu,[2] Aiqin Wang,[2] Tao Zhang,[2] Weixin Huang,[3] Junwang Tang[1*]

[1]Department of Chemical Engineering, University College London, London WC1E 7JE, UK.

[2]State Key Laboratory of Catalysis, Dalian Institute of Chemical Physics, Chinese Academy of Sciences, 116023 Dalian, China.
[3]Hefei National Research Center for Physical Sciences at the Microscale, Collaborative Innovation Center of Chemistry for Energy Materials, Key Laboratory of Surface and Interface Chemistry and Energy Catalysis of Anhui Higher Education Institutes, School of Chemistry and Materials Science, University of Science and Technology of China, Hefei 230026, China.
[4]Department of Chemical and Process Engineering, University of Strathclyde, James Weir Building, 75 Montrose Street, Glasgow, G1 1XJ, UK
[5]BCAST, Brunel University London, Uxbridge, Middlesex UB8 3PH, UK

*Correspondence to: Email: junwang.tang@ucl.ac.uk (J.T.)

Methanol with the 12.5wt% H_2 content is widely considered as a liquid hydrogen medium. Coupling with water with the 11%% H_2 content, liquid water reforming of methanol for H_2 synthesis is a promising way for on-demand hydrogen production[1]. We demonstrated an atomic-level catalyst design strategy, using synergy between single atoms and nanodots for H_2 production. The PtCu-TiO_2 sandwich photocatalyst achieved a remarkable H_2 yield (2383.9 μmol h^{-1} or 476.8 mmol g^{-1} h^{-1}) with a high apparent quantum efficiency (99.2%). Furthermore, the oxidation product is high-value chemical formaldehyde with 98.6% selectivity, instead of CO_2, leading to a nearly zero-carbon-emission process. Detailed investigations indicated a dual-role of copper atoms: an electron acceptor to facilitate photoelectron transfer to Pt, a hole acceptor for the selective oxidation of methanol to formaldehyde, thus avoiding overoxidation to CO_2. The synergy between Pt nanodots and Cu single atoms together reduced the activation energy of this process to 13.2 kJ/mol.

Hydrogen as one of the most critical energy vectors can be derived from diverse resources, including natural gas, biomass/bioalcohols and water driven by primary energy sources [2]. However, this secondary energy source suffers from transportation and storage issues. On-site synthesis of hydrogen has been reported as a promising technology to meet the requirement of the end user and to bypass such transportation and storage challenge. Among various hydrogen source feedstocks, methanol has widely been considered as the most crucial candidate due to its high mass and volume hydrogen density as well as easy transportation and storage using the

This is a peer reviewed, accepted author manuscript of the following research article: Wang, H., Qi, H., Sun, X., Jia, S., Li, X., Miao, T. J., Xiong, L., Wang, S., Zhang, X., Liu, X., Wang, A., Zhang, T., Huang, W., & Tang, J. (2023). High quantum efficiency of hydrogen production from methanol aqueous solution with PtCu–TiO2 photocatalysts. *Nature Materials* . https://doi.org/10.1038/s41563-023-01519-y

current infrastructure [3,4]. As such, the "methanol economy" suggested by Olah has long been the dream of the mankind[5].

Traditional H_2 generation from methanol steam reforming requires medium temperatures and pressures (eg. 200-350 °C, 20-50 bar), resulting in an energy-intensive process with high capital cost and high carbon dioxide emission [3,6]. Recently, liquid-phase alcohol reforming or dehydrogenation for hydrogen generation was proposed, suggesting that extracting H_2 from liquid-phase methanol was more conducive than the water-gas shift with high CO production [4]. However, the feasible heterogeneous catalysts for relatively low-temperature hydrogen production have been rarely developed. Until 2017, a benchmark catalyst Pt/MoC was reported to achieve a high hydrogen generation rate at reduced temperatures (150°C, 6 MPa) with the major oxidation product CO_2 [7]. Here we demonstrated an atomic-level catalyst design strategy, using synergy between Cu single atoms and Pt nanodots for H_2 production from methanol aqueous solution in a nearly zero-carbon emission process (nearly no CO_2 emission) at ambient pressure.

Though substantial effort has been devoted to the methanol reforming, most of the existing cases focused on the half reduction reaction with H_2 as the only interesting product, ignoring the other half oxidation reaction products which are carbon-containing products. Apart from H_2, the usage of the oxidation products such as carbon monoxide, or formaldehyde *etc.*, can be considered as an valuable approach to a circular economy [8]. Among them, formaldehyde (HCHO) is one of the most valuable chemicals as it is a versatile raw material for many chemical synthesis like dyes, plastics, and drugs [9]. Industrially, over 40% methanol has been used for HCHO production, but it again requires a relatively high temperature that comes with the by-product CO_x [10,11]. The HCHO production from methanol is currently based on Formox Process using iron molybdate catalysts [11]. However, the side reactions, especially $CH_3OH = CO + H_2$, are inevitable due to the relatively high temperature, leading to the poison of active sites by CO and high separation cost. In addition, thermal sintering was confirmed to be another severe issue for the decay of catalysts [12]. Therefore, it remains challenging to realize selective dehydrogenation of methanol to produce the oxidation product formaldehyde with high selectivity besides of reduction product H_2 under moderate conditions.

Compared with traditional thermal catalysis, photocatalysis offers a clean and sustainable way to drive chemical conversions under very mild conditions, exhibiting the great potential to address all the related issues mentioned above [13,14]. In the past several decades, photocatalytic conversion of methanol has been developed. However, the high charge carrier recombination and the lack of stable active sites resulted in a very moderate yield of hydrogen (much less than the counterpart in thermocatalysis) [15] and difficulty in controlling the selectivity of valuable by-products. Recently, engineering single-atom catalysis has become a promising strategy to achieve high efficiency and tune selectivity of products by modulating the atomic configuration to maximize metal atoms [16–18]. Among them, Cu single atom co-catalyst, was preliminarily reported as the most active non-noble metal for photocatalytic methanol conversion with the impressive H_2 evolution rate of 83.0 μmol h^{-1} [16], while the activity is still lower than the counterpart by thermal catalysis, obviously limited by the amount of Cu single atoms loaded, which is in most cases about 1% and its individual efficiency.

Hence, the development of high amount and stable single-atom catalysts remains a grand challenge. Inspired by the above-mentioned, a novel strategy was employed to obtain high concentration and evenly dispersed Cu single atoms (1.53 wt%) loaded on TiO_2 by using large surface area and porous MIL-125(Ti) as a substrate and ion-coordination method. Then Pt was immobilised on single atoms Cu to form a sandwich structure, maximising the charge transfer and more importantly stabilise active sites. The optimal PtCu-TiO_2 exhibited H_2 generation activity of 1206.5 μmol h^{-1} (241.3 mmol g^{-1} h^{-1}) (see the Movie S1) with a formaldehyde synthesis rate of 1166.0 μmol h^{-1} (233.2 mmol g^{-1} h^{-1}) and 98% selectivity at room temperature, or 2383.9 μmol h^{-1} (476.8 mmol g^{-1} h^{-1}) H_2 production rate with the nearly 100% apparent quantum efficiency at 70 °C, thus even better than the benchmark thermal catalyst for H_2 production. Of particular interest, little CO_2 was produced during for H_2 production, resulting into a nearly zero-carbon emission process. Such a special catalyst design strategy thus promises extremely efficient green H_2 production together with high value chemical synthesis under very moderate conditions.

Large surface area of MIL-125(Ti) and ion-coordination method were employed to chemically bond M species (M = Pt, Cu, Co, Ni and Ru) into the MIL-125 substrate, thus generating an extremely high concentration of M, eg. Cu single atoms on TiO_2 after calcination, which was first tested for methanol dehydrogenation at room temperature. Figure 1A represents the mass-specific H_2 generation rates achieved on MOF-derived TiO_2 loaded with various metals. All samples with co-catalysts generated a higher amount of H_2 than pristine TiO_2, following the order Cu-TiO_2 (656.7 μmol h^{-1}) > Ru-TiO_2 (304.6 μmol h^{-1}) > Ni-TiO_2 (283.6 μmol h^{-1}) > Pt-TiO_2 (254.3 μmol h^{-1}) > Co-TiO_2 (184.4 μmol h^{-1}) > TiO_2 (13.9 μmol h^{-1}), so single-atom Cu improved the H_2 production rate by nearly 50 times and was much better than widely used noble metals under the present conditions. The mechanism for this active species was investigated later. Then the optimization of Cu-TiO_2 was performed, as shown in Figure S1. As Cu increased, the activity showed a rise at the beginning, followed by a decline, indicating the amount of Cu played a critical role in the observed extraordinary activity. Increasing Cu amount increased reaction sites while too much Cu loading (>1.53 wt%) would lead to the light-shielding, limiting the generation of photo charges [28]. In addition, the synthesis conditions (solvent, annealing temperature and time *etc.*) for Cu-TiO_2 were optimized (Figure S2-S5). The Cu-TiO_2 annealed at 500 °C for 3h further improved the H_2 production rate from 656.7 μmol h^{-1} (131.3 mmol g^{-1} h^{-1}) to 777.0 μmol h^{-1} (155.4 mmol g^{-1} h^{-1}) in aqueous methanol solution (Figure S5), probably due to the optimal crystalline and Cu^+/Cu^{2+} ratio obtained in such condition. When further increasing calcination temperature and time, the activity of TiO_2 indicated a decrease. One reason might be that the Cu^+/Cu^{2+} ratio changed dramatically as discussed later.

To confirm the origin of the enhanced activity, MIL-125 derived TiO_2 was prepared at various temperatures (Figure S6). From the XRD result, as the temperature increased from 450 °C to 600 °C, the rutile phase increased. All these TiO_2 exhibited the H_2 yield ranging from 9.2 to 15.9 μmol h^{-1}, indicating that comparing with TiO_2 prepared at same temperature of 500 °C, the 60 times higher activity of Cu-TiO_2 (777.0 μmol h^{-1}) was due to the Cu species introduction. In addition, Pt-TiO_2 obtained by a widely used photodeposition method was also tested for comparison, it exhibited a high activity of 684.5 μmol h^{-1}, while still smaller than Cu-TiO_2 obtained from MIL-125 ion-coordination method, again indicating the single atom Cu loaded TiO_2 was the best under the current experimental conditions.

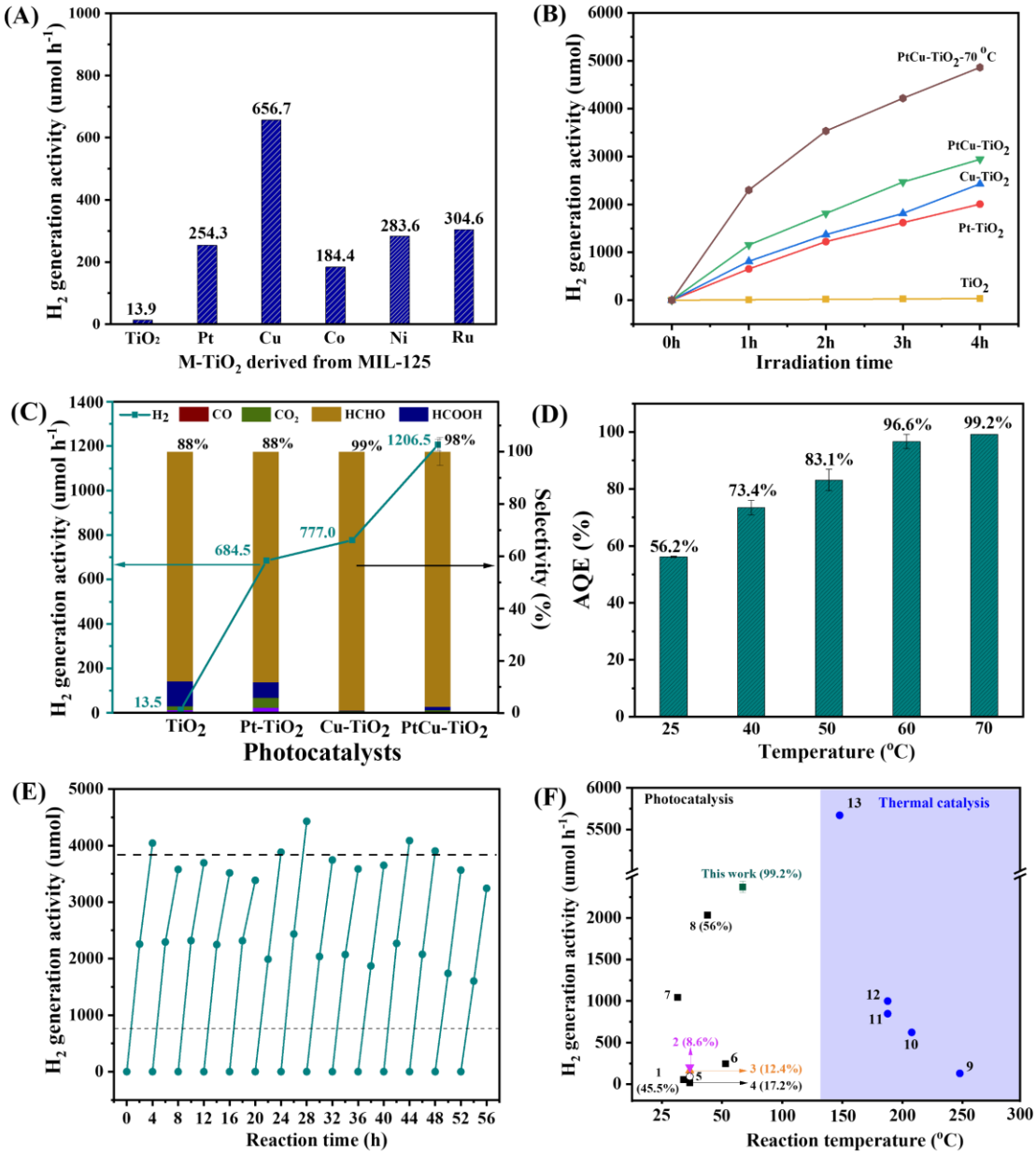

Figure 1 | H_2 production from liquid water reforming of methanol by photocatalysis. A, The mass-specific H_2 generation rates achieved on MOF-derived TiO_2 loaded with various metals, herein Cu served as the most efficient reaction sites. Herein M-TiO_2 was calcined at 450 °C for 4h. **B**, Photocatalytic activity of the single atom or bimetallic species, indicating that PtCu co-loading remarkably improved the activity. Cu-TiO_2 was prepared at 500 °C for 4h. **C**, The products selectivity of different catalysts, showing the formaldehyde (whose selectivity was shown by orange colour) was the main oxidation product and the selectivity over PtCu-TiO_2 was up to 98%. **D**, The apparent quantum efficiency (AQE) of the optimal PtCu-TiO_2 at low temperatures with the error bar, close to 100% quantum efficiency achieved. **E**, 7-day run of stability test of the PtCu-TiO_2 catalyst (each day run 2 cycles during daytime). **F**, The activity summary of the reported benchmark photo- and thermo- catalysts clearly indicates that PtCu-TiO_2 remarkably outperformed all photocatalysts and was comparable to the best thermal catalysts.

(1) $_{0.75\%}$Cu-TiO_2 [16], (2) i-Pt-TiO_2 [20], (3) $Ni(OH)_2/TiO_2$ [21], (4) $_{34\%}$Cu-TiO_2 [22], (5) $_{3\%}$Li-TiO_2 [23], (6) FP-$_{0.5\%}$Pt-TiO_2 [24], (7)$_{0.188\%}$Pt-NYTiO_2 [25], (8) $_{1.5\%}$Cu- TiO_2 [19], (9) Pt-TS-1 zeolite [26], (10) Cu-Zn-Ti [27], (11) $_{2\%}$Pt-TiO_2 [7], (12) $_{2\%}$Pt-Al_2O_3 [7], (13) $_{2\%}Pt_1$ /MoC [7]. The quantum efficiency of all representative photocatalysts were indicated in the parenthesis behind.

Pt was then introduced to further promote the activity and more importantly the stability via the synergy between Cu and Pt [29]. Pt increased Cu-TiO_2 activity to 1206.5 μmol h^{-1} (241.3 mmol g^{-1} h^{-1}) H_2 when its loading amount was 0.5 wt% (Figure S7). The optimised PtCu-TiO_2 showed 89 times higher activity than the pristine TiO_2 at room temperature. Figure 1B and Figure S8 show the initial catalytic activity change with time over different photocatalysts with an order of PtCu-TiO_2 (1206.5 μmol h^{-1} or 241.3 mmol g^{-1} h^{-1}) > Cu-TiO_2 (777.0 μmol h^{-1} or 155.4 mmol g^{-1} h^{-1}) > Pt-TiO_2 (684.5 μmol h^{-1} or 136.9 mmol g^{-1} h^{-1}) > TiO_2 (13.5 μmol h^{-1} or 2.7 mmol g^{-1} h^{-1}). The observed activity of Pt-TiO_2 and Cu-TiO_2 was much higher than pure TiO_2, ascribing to the co-catalyst loading. It should be noted that Cu-TiO_2 exhibited higher activity than all of them including Pt-TiO_2, ascribing to the bifunctional Cu species where Cu^{2+} acted as an electron acceptor for H_2 generation and Cu^+ served as a hole extraction site for methanol oxidation as proved later.

Furthermore, the activity of PtCu-TiO_2 was tested at different temperatures, from 25 °C to 70 °C (Figure S10), which exhibited an increasing trend with the rise of temperature. The control experiment showed no generation of H_2 at 70°C under the dark condition, ruling out the thermal catalysis contribution under this experimental condition. Next, Figure 1C shows the oxidation product selectivity of methanol dehydrogenation over the optimised photocatalyst and reference photocatalysts. HCHO was the main oxidation product, along with only a trace amount of CO and CO_2. The reference TiO_2 excited a selectivity of 80% toward HCHO, similar to the reported selectivity of the TiO_2[30–32] . Compared with pure TiO_2, the introduction of Pt on TiO_2 did not increase the selectivity to formaldehyde while single atoms Cu increased the selectivity to 99%, probably due to the mitigated overoxidation by Cu introduction. PtCu-TiO_2 showed a similar selectivity to Cu-TiO_2 (up to 98.6%), further suggesting the vital role of Cu atoms, with the formaldehyde synthesis rate of 1871.5 μmol h^{-1} (374.3 mmol g^{-1} h^{-1}) at 60 °C and 2259.5 μmol h^{-1} (451.9 mmol g^{-1} h^{-1}) at 70 °C (Figure 1B). The selectivity to other oxidation products was 0.77% for HCOOH, 0.56 % for CO_2, and 0.06 % for CO when operating at 70 °C. The apparent quantum efficiency is the most reliable criterion for photocatalysis, which was determined in Figure 1D. One can see that the AQE reached 96.6-99.2% at the temperature of 60-70 °C, a record in this area.

The reducibility and stability of the photocatalyst are very important. In most cases, a few hours or maximum one day photocatalysts' stability were reported [33–35]. Herein PtCu-TiO_2 stability was studied by 7 consecutive day runs (as H_2 production rate was too high so we had to stop experiments in the nighttime for the safety reason) (Figure 1E). PtCu-TiO_2 exhibited a steady activity over 14 cycles, suggesting the excellent stability and activity of the photocatalyst. The slight activity fluctuation was likely due to the methanol concentration changing caused by the process of purging and catalyst particles stuck to the stirring bar. In comparison, the stability of the present Cu-TiO_2 was also investigated, which showed an obvious decrease, reducing activity by more than 60% after five cycles (Figure S11). MP-AES and XPS measurements of Cu-TiO_2 and PtCu-TiO_2 before and after 20h reaction were carried out to investigate the reason for the

decreased activity of Cu-TiO_2. The MP-AES result (Table S1) revealed the metal (Pt and Cu) amount almost remained unchanged, excluding the possibility of Cu single atom leaching. From XPS Cu 2p spectra (Table S2), the Cu^{2+} concentration of Cu-TiO_2 decreased from 38.5% to 19.2% after 20 hour reaction while there was negligible change of Cu^{2+}/Cu^{+} ratio in PtCu-TiO_2 before and after the photocatalytic reaction. This was attributed to the function of Pt as an efficient electron acceptor, thus stabilising the regeneration of Cu^{2+} during photoreaction. On the other hand, most Cu^{2+} was not recovered during photocatalysis over Cu-TiO_2, which could explain the reduced activity. From Pt 4f spectra before and after the reaction, there was no change observed. The results also evidenced that the Pt nanodots loading enabled Cu to be both more active and stable than pure Cu species, assuring the long-term stability of PtCu-TiO_2.

The activity of PtCu-TiO_2 was also compared with the reported efficient catalysts in methanol-dehydrogenation by both photocatalysis and thermal catalysis (Figure 1F and Table S3). PtCu-TiO_2 represented a remarkably high activity, eg. 1206.5 μmol h^{-1} **(**241.3 mmol g^{-1} h^{-1}**)** and 2383.9 μmol h^{-1} **(**476.8 mmol g^{-1} h^{-1}**)** at 25 ºC and 70 ºC, respectively, much higher than the reported photocatalysts (Table S3) so far. Such a H_2 evolution activity is also comparable to the benchmark Pt/MoC operated at 150 ºC and under 6 MPa, where CO_2 was produced as the major oxidation product[7]. Different from the benchmark thermal catalysis, high valuable chemical formaldehyde was synthesized in this study (Table S4). The activation energy is a key indicator to reflect whether a catalyst is efficient or not, thus an Arrhenius plot was conducted to estimate the activation energy for hydrogen generation reaction by the photocatalysts [36], as shown in Figure S12. In this case, the activation energy of TiO_2 and PtCu-TiO_2 were estimated to be 35.2 kJ mol^{-1} and 13.2 kJ mol^{-1}. Compared with pure TiO_2, nearly one-third of activation energy measured on PtCu-TiO_2 strongly indicated that the PtCu greatly promoted the H_2 production, matching well with the observed activity.

Then we investigated the structure and morphology of the most advanced photocatalyst (PtCu-TiO_2) to understand the underlying reason for such high efficiency and AQE. A series of characterisations were carried out. The X-ray powder diffraction (XRD) was used to analyse the crystallinity and phase composition of Cu-TiO_2, shown in Figure 2A. The XRD spectrum presented the mixed-phase of anatase and rutile of MOF-derived TiO_2 while Cu-TiO_2 showed the pure anatase phase although they were calcined at the same temperature of 500 ºC, suggesting the anchor of Cu species might stabilise the anatase phase [37]. The spectra revealed that higher calcination temperature resulted in more rutile formation. No characteristic peaks associated with Cu were observed in all Cu-TiO_2 samples although the high amount of 1.53% Cu was loaded, attributing to the highly dispersed Cu species. In addition, Raman spectroscopy was performed to confirm the phase of Cu-TiO_2, shown in Figure 2B. The $E_{g(1)}$, $E_{g(2)}$, B_{1g}, A_{1g}, $B_{1g(2)}$ and $E_{g(3)}$ were assigned to anatase TiO_2, where the E_g, B_{1g}, A_{1g} mode belonged to symmetric stretching, symmetric bending and antisymmetric bending vibration of O-Ti-O bonding, respectively [38]. As the temperature increasing, all samples started to exhibit vibrational modes at 445 cm^{-1}, and the

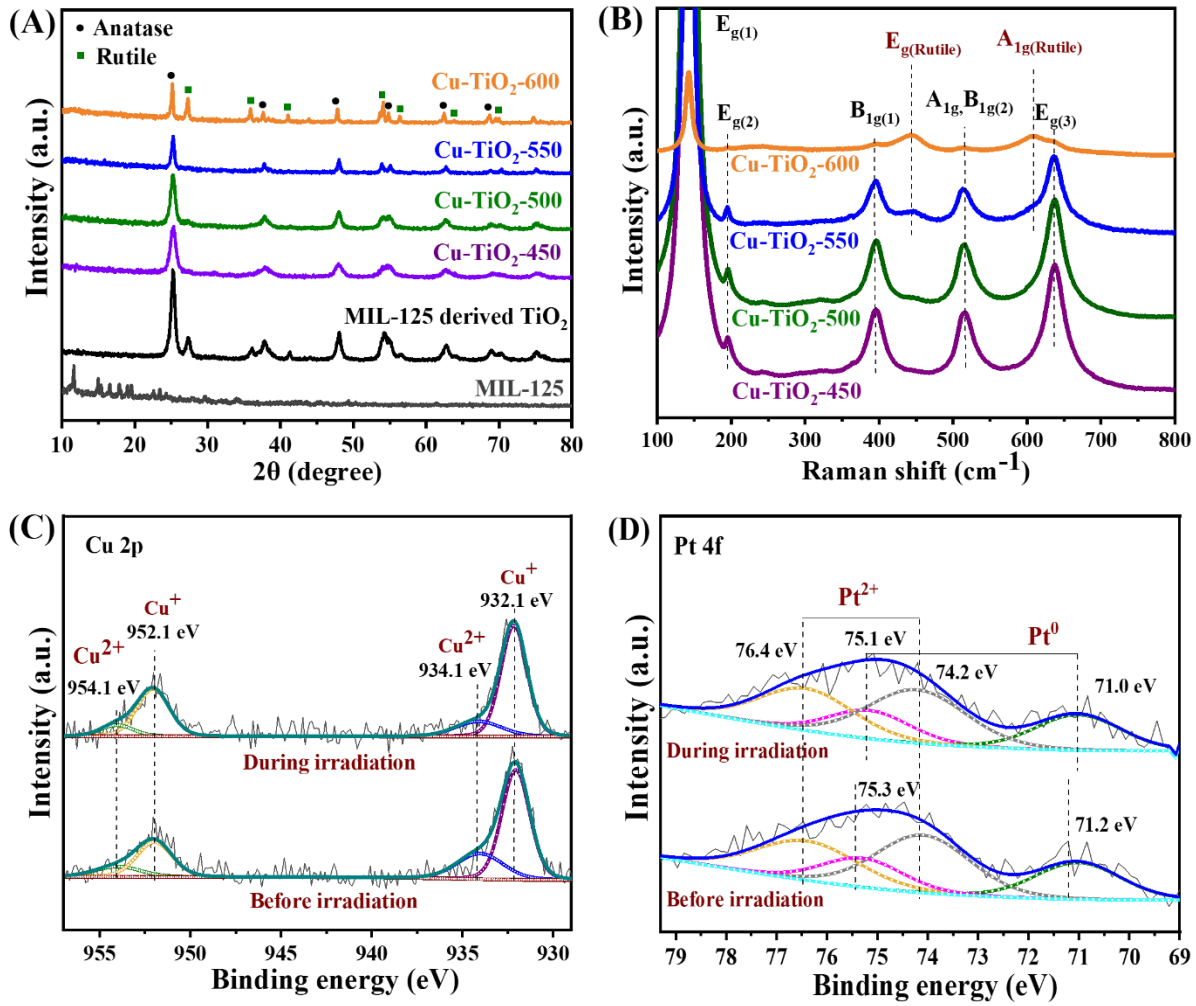

Figure 2 | Physical characterisation of the photocatalysts. A, XRD and **B**, Raman spectra of TiO_2 and Cu-TiO_2. **C**, The in-situ XPS Cu 2p spectra of PtCu-TiO_2 before and during irradiation, indicating that Cu^{2+} was in-situ reduced to the active site Cu^{+}. **D**, The XPS Pt 4f spectra of PtCu-TiO_2 before and during irradiation.

signal at 608 cm^{-1} kept arising from 500 ^{o}C to 600 ^{o}C. This phenomenon demonstrated that the primary bonding environment of anatase remained unchanged, but more rutile TiO_2 appeared when further heating, in line with XRD.

Then the scanning electron microscope (SEM) and transmission electron microscopy (TEM) were carried out to investigate the morphology of TiO_2 and PtCu-TiO_2. The pristine TiO_2 (Figure S13A-B) presented a disk-type shape in the 200-500 nm range, while PtCu-TiO_2 (Figure 3A, Figure S13C-D) remained a similar morphology with a rougher surface due to the deposition of PtCu. Furthermore, TEM of PtCu-TiO_2 (Figure 3B) revealed that the disk-like PtCu-TiO_2 was nanoporous and the bright dots on TiO_2 matrix were assigned to Pt dots with a diameter around 1-3 nm. The observed lattices (Figure 3C and Figure S14) were 0.35 nm, 0.18nm and 0.26 nm corresponding to TiO_2 (101), TiO_2 (200) and Pt (111), respectively, matching well with the corresponding diffraction. To reveal the Cu state in PtCu-TiO_2, the profiles of two lines were shown in Figure 3D. Line 1 only showed Ti atoms, while line 2 contained both Ti and Cu atoms,

indicating the highly dispersed Cu atoms in TiO_2 (Figure 3E and Figure S15). The STEM-EDS mapping (Figure 3G) represented the uniform distribution of Ti, O, Cu, confirming Cu was high dispersed in the TiO_2 substrate, while Pt concentration was much less than Cu. To further verify the PtCu formation, the point analysis from energy-dispersive X-ray spectroscopy was performed (Figure S16). The marked region with green (point 1 and 3) showed that these brighter dots were Pt and Cu-rich, while the blue region (point 2 and 4) was only composed of Cu. The aberration-corrected high-angle annual dark-filed scanning transmission electron microscopy (AC-HAADF-STEM) analysis was then performed on an equivalent sample of Rh-TiO_2. From Figure S17, bright single atoms assigned to Rh were highly distributed on the surface of TiO_2, confirming the successful preparation of Rh single atoms via this method. This also suggested that Cu single atom would exist on the surface of TiO_2.

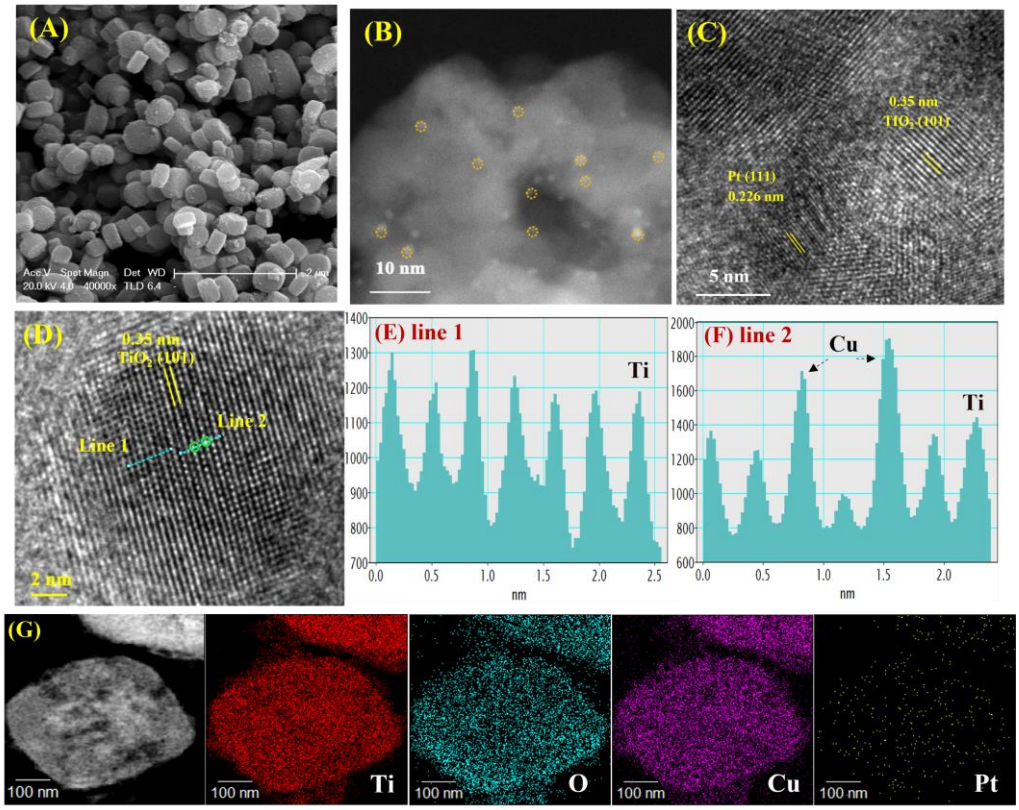

Figure 3 | Morphology observation of the catalysts. **A**, SEM, **B**, STEM with Pt marked by yellow circles, **E-D**, high revolution TEM of PtCu-TiO_2 with TiO_2 (101) and Pt (111) crystalline, indicating the formation of PtCu-TiO_2. The corresponding line scan profile marked in **D**, with **E** blue lines 1 (only Ti) and **F** line 2 (with two bright points of Cu atoms marked by green circles). **G**, STEM of PtCu-TiO_2 and the corresponding element mapping, showing much more highly dispersed Cu than Pt in the catalyst.

The X-ray absorption near-edge structure (XANES) and extended X-ray absorption fine structure (EXAFS) were used to further investigate the electronic state and local coordination environment of Cu and Pt in the samples. From the XANES spectra at the Cu K-edge (Figure S18), The edge energies (E_0) for Cu-TiO_2 and PtCu-TiO_2 samples were between that of CuO and of Cu_2O, suggesting that Cu species possessed a combined feature of Cu^+ and Cu^{2+} and it matched with the XPS result below. Moreover, the Fourier-transformed k^2-weighted EXAFS spectra of the Cu

K-edge (Figure 4A) showed that the position at 1.5 **Å** (not corrected in the phase) was assigned to C–O shell of CuO, while two peaks at 2.45 **Å** and 2.73 **Å** (not corrected in the phase) corresponded to Cu-O-Cu of the reference Cu_2O. Note that the main peak of Cu-O bond for both Cu-TiO_2 and PtCu-TiO_2 was located at the mid of CuO and Cu_2O, indicating that Cu species in samples carried the mixed feature of Cu^+ and Cu^{2+}. Moreover, no Cu-Cu and the second shell Cu-O-Cu configuration were observed, confirming the isolated Cu atoms existed in the catalysts. Furthermore, the EXAFS data-fitting results (Table S5) showed that the Cu–O coordination number (CN=3.4 for PtCu-TiO_2 and CN=3.5 for Cu-TiO_2) was quite different from that of CuO (CN=4), Cu_2O (CN=2) and Cu-Cu bond (CN=12), indicating the atomic level of Cu species in PtCu-TiO_2 and Cu-TiO_2. Moreover, the binding length Cu-O in PtCu-TiO_2 (1.94 Å) was very close to that of standard CuO, probably due to the presence of Pt enabled the recovery of Cu^{2+}. From XANES spectra of the Pt LIII-edge (FigureS19), PtCu-TiO_2 exhibited a slightly E_0 shift compared with reference Pt foil, which might be ascribed to Pt-Cu formation or partial oxidation of Pt. The Fourier-transformed k^2-weighted EXAFS spectra of the Pt L_{III}-edge revealed that the Pt-Pt shell profile (Figure 4B) of PtCu-TiO_2 (2.3 **Å**, not corrected in the phase) was slightly different to that of Pt foil (2.4 **Å**, not corrected in the phase), probably attributing to the presence of Pt-Cu bond. Further EXAFS data-fitting (Table S5) showed that there were three neighbouring shells in PtCu-TiO_2: Pt-Pt (CN = 8.5), Pt-Cu (CN = 2.4), and Pt-O (CN = 0.9), consistent with the elementary mapping. As speculated, Pt-Cu formation may result in electron transfer between Pt and Cu atoms. The wavelet transform (WT) analysis was then performed to further determine the coordination environment of Cu and Pt on the TiO_2 surface. As shown in Figure S20A-B, Cu foil afforded lobe at (2.3 Å, 7.3 $Å^{-1}$) for Cu–Cu coordination, and CuO reference afforded two lobes at (1.4 Å, 5.0 $Å^{-1}$) and at (2.5 Å, 4.5 $Å^{-1}$) for Cu-O and Cu-O-Cu coordination, respectively. The absence of such a lobe at high k value in Cu-TiO_2 and PtCu-TiO_2 (Figure S20C-D) indicated that predominant Cu was isolated and the individual atom surrounded by Pt atoms in Cu-TiO_2 and PtCu-TiO_2. On the contrary, a lobe at low k values (1.4 Å, 5.0 $Å^{-1}$) and (2.5 Å, 3.6 $Å^{-1}$) were observed, which can be attributed to Cu–O ad Cu-O-Ti coordination. Similarly, as shown in Figure S21A-B, Pt foil showed a lobe at (2.7 Å, 10.4 $Å^{-1}$) for Pt-Pt coordination, while PtO_2 exhibited a lobe at (1.6 Å, 6.4 $Å^{-1}$) and (3.0 Å, 11.2 $Å^{-1}$) for Pt-O-Pt coordination. The absence of former lobes in PtCu-TiO_2 might be due to the low concentration of Pt-Pt. Instead, for the WT contour plot of PtCu-TiO_2 (Figure S21C), one broad lobe at (2.4 Å, 7.0 $Å^{-1}$) was observed, probably assigned to combination of Pt-Cu and Pt-Pt contribution. There existed a tiny lobe at (1.6 Å, 5.7 $Å^{-1}$) for Pt–O coordination, due to the partial Pt oxidation. In brief, EXAFS results supported that highly dispersed Cu single atoms were partially coupled with Pt dots in the PtCu-TiO_2 sample while the other single atoms Cu existed as Cu-O species.

The in situ X-ray photoelectron spectroscopy (XPS) of PtCu-TiO_2 during the photocatalytic process was performed to study the compositional changes (Figure 2C). The control experiment using PtCu-TiO_2 before irradiation was carried out as a reference. The peaks at 932.1 eV and 952.1 eV were attributed to Cu^+ while the other peaks at 934.1 eV and 954.1 eV were assigned to Cu^{2+}. The spectra evidenced that Cu^+ and Cu^{2+} coexisted in Cu-TiO_2 and PtCu-TiO_2 [39]. During irradiation, the ratio of Cu^+/Cu^{2+} showed an increase from 2.60 to ca. 4.05, clearly revealing that Cu^{2+} trapped electrons in the process. For Pt 4f (Figure 2D), the observed binding energy of Pt $4f^{5/2}$ and Pt $4f^{7/2}$ were 71.2 eV and 75.3 eV, corresponding to Pt^0. While the binding energy of 74.2 eV and 76.4 eV corresponded to the Pt^{4+}, which might be due to the oxidized state (PtO_2) [40]. The Pt/Pt^{4+} during irradiation remained the same but the binding energy of Pt^0 shifted by 0.2 eV

toward lower binding energy, suggesting that Pt surface became electron-rich [41]. In addition, the binding energy of Pt^{4+} remained almost the same, indicating that the electrons were trapped by Pt^0 instead of Pt^{4+}. The result suggested that only Pt located on the Cu species could extract photoelectrons, likely from Cu^+ to become electron-rich sites. This proved the synergy between Cu and Pt for a remarkably stable catalytic process. In addition, the elemental chemical states and surface composition of Cu-TiO_2 prepared from different temperatures and PtCu-TiO_2 were investigated (Table S6). PtCu-TiO_2 exhibited a higher Cu^+/Cu^{2+} ratio of 2.60 than the ratio of 1.60 in Cu-TiO_2, which was believed due to the conversion of Cu^{2+} to Cu^+ during Pt photodeposition, consistent with the EXAFS spectra of Pt. Moreover, the peak attributed to the Cu^+ state continued to decrease while Cu^{2+} kept increasing when temperature increased, suggesting that further heating facilitated Cu^{2+} formation. The correlation between Cu^+/Cu^{2+} ratio and H_2 yield were shown in Figure S22, which represented high H_2 production rates could be attained when Cu^+/Cu^{2+} ranged from 0.64 to 1.60, might revealing that both Cu^+ and Cu^{2+} were the active sites.

The UV-vis diffuse reflectance spectra of TiO_2, Cu-TiO_2 and PtCu-TiO_2 were shown in Figure S23, where loading both Cu and Pt exhibited a similar band absorption to TiO_2. Electron paramagnetic resonance (EPR) was performed to investigate the chemical state of Cu species and the charge transfer direction, shown in Figure 4C. Cu-TiO_2 and PtCu-TiO_2 exhibited similar strong peaks attributing to I = 3/2 of Cu^{2+} [42]. Upon irradiation, the decreased intensity of the Cu^{2+} signal implied Cu^{2+} trapped electrons to form an EPR-silent Cu^+. PtCu-TiO_2 showed the same trend but weaker intensity reduction (insert in Figure 4C), revealing that the electrons further transferred from Cu^+ to Pt, leading to the subsequent partial Cu^{2+} recovery or that original Cu^+ was oxidised to Cu^{2+} by holes. In addition, the photoelectrochemical study was performed to investigate the charge carrier transfer (Figure S24-26). The anodic photocurrent (Figure S25) of Cu-TiO_2 was much higher than that of TiO_2, indicating that Cu co-catalyst could facilitate water /methanol oxidation or work as hole acceptors on the anode, likely due to the existence of Cu^+ in the sample. Pt and Cu both loading further increased anodic photocurrent a little as the major contribution was from isolated Cu^+ ions. The electrochemical impedance spectra (EIS, Figure S26) exhibited that PtCu-TiO_2 had the smallest resistance. The decreased Rct and R_{Bulk} indicated the enhanced charge transfer and accelerated kinetics of water oxidation, which was consistent with the photocurrent. A similar phenomenon was also observed by the time-resolved photoluminescence (Figure S27 and Table S7). The PL lifetime τ of TiO_2 was 1.02 ns. Either Pt or Cu loading increased lifetime τ, while Pt was more efficient (1.37 ns of Pt-TiO_2 > 1.12 ns of Cu-TiO_2). The co-loading of Pt and Cu represented the second-longest lifetime (1.25 ns), indicating Pt efficiently traps electrons from TiO_2 via Cu. Although the Pt-TiO_2 exhibited the most efficient photoelectrons transfer, its H_2 generation rate was much lower than that of Cu-TiO_2 and PtCu-TiO_2. This was very likely due to both electron acceptors of Cu^{2+} species and hole acceptors of the Cu^+ species in the single atoms Cu loaded photocatalyst, which could facilitate the whole catalytic cycle with very small activation energy. Unlike previous reports, our results imply the importance of bifunctional Cu species in this reaction for photocatalytic hydrogen production and formaldehyde synthesis, together with the synergy between Cu single atoms and Pt nanodots.

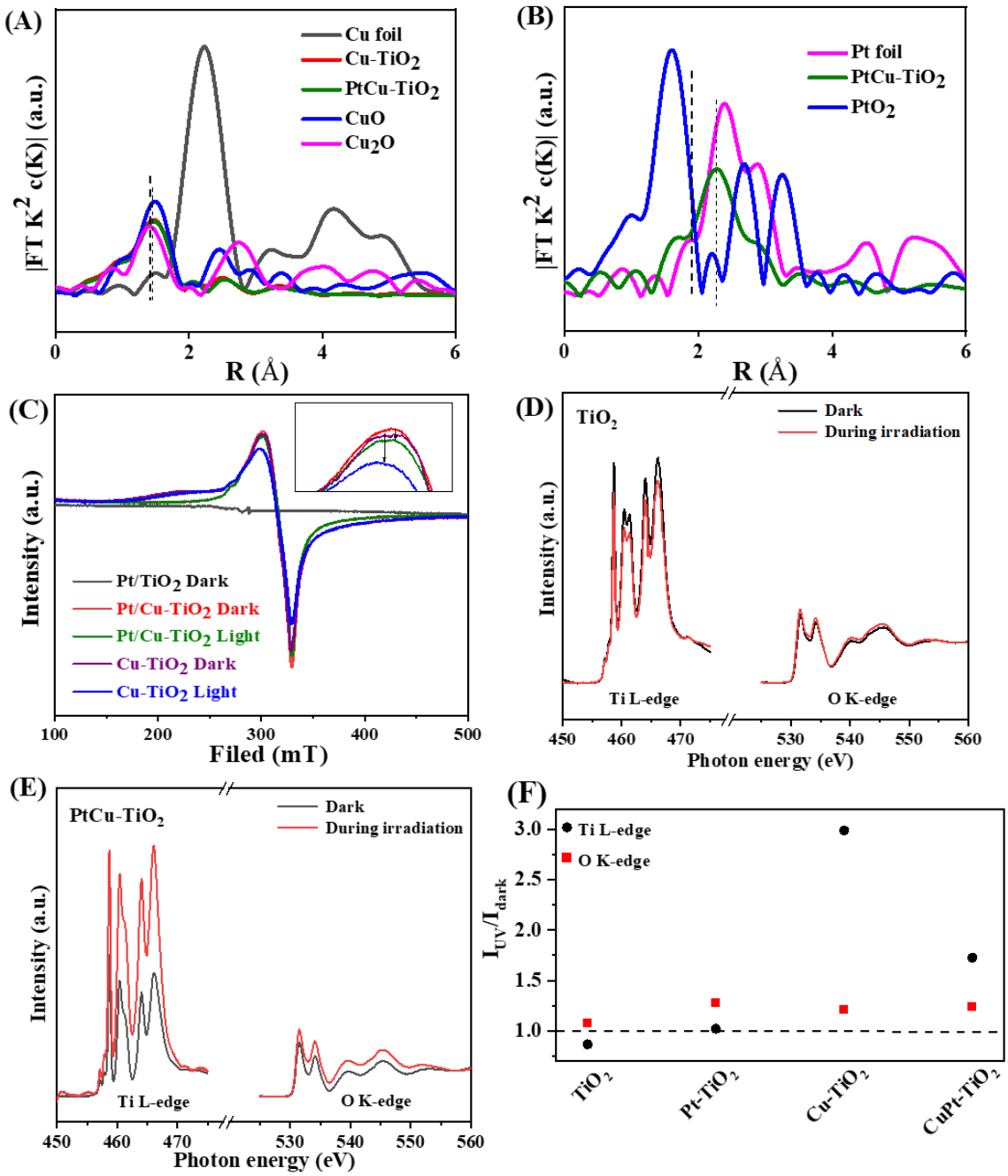

Figure 4 | Chemical characterisation of the photocatalysts. **A**, The Fourier transform of k^2-weighted EXAFS spectra at the K-edge of Cu-TiO_2, PtCu-TiO_2, Cu foil and CuO. **B**, The Fourier transform of k^2-weighted EXAFS spectra at the LIII-edge of Pt-TiO_2, PtCu-TiO_2, Pt foil and PtO_2. **C**, The electron paramagnetic resonance (EPR) of Pt-TiO_2, Cu-TiO_2 and PtCu-TiO_2. The Cu^{2+} signal decrease was more evident in Cu-TiO_2 than PtCu-TiO_2 (Insert), indicating that the electrons likely further transferred from Cu^+ to Pt, leading to the partial Cu^{2+} restoring. Ti L-edge and O K-edge EXAFS spectra of **D**, TiO_2, and **E**, PtCu-TiO_2 under dark and during irradiation. **F**, Ratio of Ti L-edge or O K-edge intensity in the modified samples under light irradiation to that under dark condition.

To further investigate the synergy of Cu and Pt, the operando UV−vis−NIR diffuse-reflectance spectroscopy analogous to the time-zero measurement in transient absorption spectroscopy was carried out under controlled atmospheres. Argon, dry air, and methanol vapor atmospheres were used as an inert reference, an electron acceptor, and a hole acceptor, respectively. Such operando technique can directly observe the charge transfer between the co-catalysts and TiO_2 and reactions between photoexcited charges and reactants [43,44]. The photoinduced absorption in the NIR region under different atmospheres is shown in Figure 4. The observed absorption across the NIR region was believed to be dominated by photo-excited electrons while photoholes absorption was used to be at short wavelengths (400-500 nm) which was not reliable to be monitored by here due to the small signal to noise [45]. Under argon conditions (Figure 4A), pure TiO_2 as a reference showed a positive % abs signal under 365 nm excitation. Cu-TiO_2 exhibited a much smaller % abs signal compared with pure TiO_2, which was consistent with the trapping of electrons by Cu^{2+} as observed by in-situ XPS and EPR. In addition, the electron signals almost disappeared when anchoring Pt or PtCu on TiO_2, indicating that the electron capture by Pt or PtCu was more efficient than that of Cu. A close observation of these curves would find PtCu was more efficient than Pt for electrons trapping. Such phenomenon might be assigned to the large work function of Pt [46] and strong interaction between Cu and Pt as observed by HRTEM and EXAFS so that electron could be injected to Pt via Cu. When argon was replaced with the dry air where O_2 gas was a good electron scavenger (Figure 4), the dramatically reduced signal in TiO_2 indicated that the photo-induced electrons were quenched by oxygen (oxygen reduction). The absorption spectra of Pt-TiO_2 and PtCu-TiO_2 changed a little under air compared with that under argon. More interestingly, spectra of Pt-TiO_2 and PtCu-TiO_2 were weaker than TiO_2 under air, suggesting that Pt and PtCu played the more efficient role for oxygen reduction. This suggested they could reduce proton efficiently as proton reduction is thermodynamically and kinetically easier than oxygen reduction. In the presence of methanol as an efficient hole scavenger (Figure 4C), the photoinduced absorption of the reference TiO_2 remarkably enhanced compared with that under argon condition (Figure 4A), as electrons accumulated after those photoholes were consumed by methanol. The signals of Cu-TiO_2, Pt-TiO_2 and PtCu-TiO_2 under methanol condition were similar to that under argon condition, revealing that Cu, Pt and PtCu served as efficient electron capture sites even though photoholes were efficiently consumed by methanol, highly matched with the electron transfer pathway suggested.

In situ EXAFS was also performed to probe the density of orbital states involved in the electron transitions, thus revealing the charge transfer pathway. Ti L-edge and O K-edge EXAFS absorption features of TiO_2, Pt-TiO_2, Cu-TiO_2, PtCu-TiO_2 were acquired under dark and during irradiation (Figure 4D-F). The band structure of TiO_2 involves Ti 3*d* and O 2*p* orbitals, where Ti L-edge probes electron transition Ti $2p \rightarrow 3d$ and O K-edge presents electron transition O $1s \rightarrow 2p$, reflecting the density of unoccupied Ti *3d* and O *2p* states, respectively. Figure S29A shows the dark states of Ti L-edge and O K-edge EXAFS of TiO_2, Pt-TiO_2, Cu-TiO_2, PtCu-TiO_2 and Figure S29B exhibits the ratio of modified samples vs. TiO_2. From Figure S29B, Ti L-edge ratio of Pt-TiO_2 to TiO_2 exhibited a value lower than 1, indicating that electrons flowed from Pt to TiO_2 under dark condition and thus there was a less-unoccupied Ti 3*d* orbital in Pt-TiO_2, consistent with the previous observation that electrons in Pt can transfer back to TiO_2 [45]. Comparatively, Cu-TiO_2 and PtCu-TiO_2 presented evidently higher ratios than 1, indicating a reverse electron flow direction. In other words, both Cu^{2+} and PtCu worked as an one-way electron acceptor or electrons could not move back to TiO_2 from PtCu or Cu^{2+}. On the other hand, Cu^{+} could induce

oxygen vacancies, leading to an increased O K-edge on both Cu-TiO_2 and PtCu-TiO_2 but not on Pt-TiO_2. Light irradiation induced charge excitation, thus affecting the density of Ti *3d* and O *2p* orbital states. As shown in Figure 4D, TiO_2 exhibited a weak Ti L-edge signal, which was attributed to the electron excitation from O *2p* to Ti *3d* under irradiation and led to a more-occupied Ti 3*d* orbital. The intensity ratio under irradiation against dark (I_{UV}/I_{dark}) of Ti L-edge follows the order Cu-TiO_2 > PtCu-TiO_2 > Pt-TiO_2 > TiO_2, as shown in Figure 4F. A slightly bigger I_{UV}/I_{dark}(Ti L-edge) was observed in Pt-TiO_2, indicating that Pt could act as an electron trapping site. Impressively, Cu-TiO_2 exhibited the largest I_{UV}/I_{dark}(Ti L-edge) value, indicating Cu could most effectively abstract electrons from TiO_2. Considering electrons could backflow from Pt to TiO_2 under dark condition as discussed above, the slight enhanced Ti L-edge intensity in Pt-TiO_2 was reasonable due to the two-way flow of electrons. The I_{UV}/I_{dark} (Ti L-edge) of PtCu-TiO_2 was also bigger than Pt-TiO_2 but smaller than Cu-TiO_2, which was due to the combination effect of Cu and Pt involving both one way electron capture and electron backflow. This supported the claim that single-atom Cu^{2+} species were inserted between Pt and TiO_2, so Cu^{2+} species in PtCu-TiO_2 could not only accept the electrons and transfer them to Pt but also mitigate the electron backflow form Pt to TiO_2. All samples showed increased O K-edge absorption under irradiation, but with various intensity changes, which was ascribed to the combination of charge excitation and the charge transfer. A slightly increased O K-edge feature was presented in TiO_2 (Figure 4D), arising from a less-occupied O 2p orbital caused by the photoexcited electrons excitation. The I_{UV}/I_{dark} (O K-edge) value of Pt-TiO_2 was the largest, as the electrons were excited from O2p to Ti 3d, then transfer to Pt, leading to a much less-occupied O *2p* orbital. Interestingly Cu-TiO_2 with the one way electron trapping ability had a smaller I_{UV}/I_{dark}(O K-edge) than Pt-TiO_2, which was believed due to that Cu^+ worked as the efficient hole capture site besides Cu^{2+} as an electron acceptor. As such, holes in O 2p orbital after the electron excitation were abstracted by Cu^+, reducing possibility of O K-edge absorption. A similar case existed in PtCu-TiO_2, where its I_{UV}/I_{dark} (O K-edge) was very close to that of Cu-TiO_2, further suggesting the role of Cu^+ for hole trapping. All these in situ results clearly indicated that PtCu was an efficiency electron sink, and the proposed charge flow was described in Figure S31. In addition, Density Functional Theory (DFT) calculation was performed to present the reaction pathway (Figure S32-33), where electrons transfer to Cu^{2+} followed by the mobility to Pt for H_2 evolution and meanwhile CH_3OH oxidation occurs in Cu^+ site.

A reaction scheme for methanol conversion on PtCu-TiO_2 is thus proposed in 1. When electrons and holes are excited in TiO_2 followed by charge carrier transfer. Single-atom Cu^{2+} species trap the electrons to form Cu^+ sites. Then, the electrons migrate to Pt as a reduction reaction site and meanwhile the Cu^+ species recover to Cu^{2+}. In parallel, the left holes are extracted by the Cu^+ species in another site of TiO_2 surface to form Cu^{2+} that is the oxidation reaction site, which has a moderate oxidation potential compared with photoholes themselves in the valance band of TiO_2, avoiding overoxidation of methanol to CO_2. One can see that the Cu^{2+}-Pt is for the electron trapping while the Cu^+ is responsible for the hole trapping. Next the reduction and oxidation reactions occur in the corresponding active sites. In detail, protons (H^+) are reduced into H_2 in the electron-rich Pt (e^-) sites and the dispersed Cu^{2+} react with methanol to produce formaldehyde. After the reaction, the catalyst recovers to the original state. Based on the

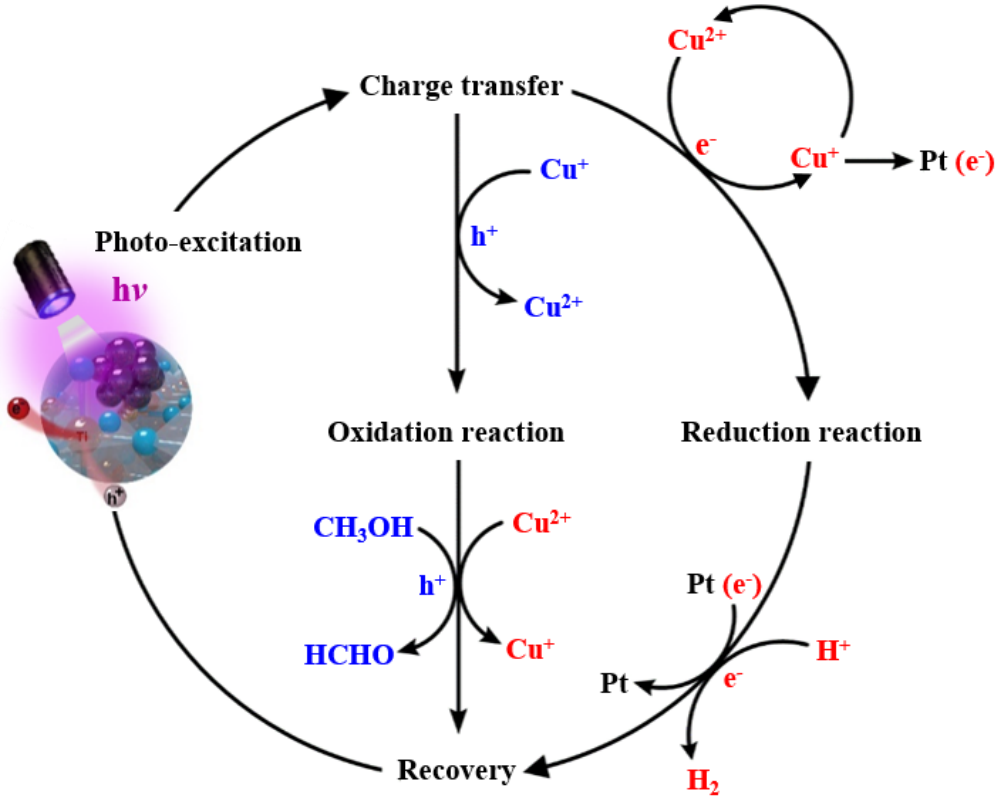

Scheme 1 | The possible mechanism of photocatalytic methanol conversion on PtCu-TiO_2 for both H_2 and valuable chemicals production instead of CO_2

observed performance and characterization results, the extraordinary H_2 production activity obtained by PtCu-TiO_2 can be ascribed to the following reasons. On the one hand, the MIL-125 as a template provides substantial sites for chemically Cu anchoring, maximizing single atom loading for the efficient electron capture. Then the controlled annealing ensures mixture of Cu^{2+} and Cu^{+} species. Pt loading helps proton reduction and regeneration of Cu^{2+}. On the other hand, the atomic hole acceptor (Cu^{+}) for selective methanol oxidation to formaldehyde plays an important role, avoiding the overoxidation to CO_2 or CO by photoholes in the valance band of TiO_2, leading to a nearly zero CO_2 process. Such a favourable synergetic effect between Pt nanodots and mixed Cu atomic species promotes charge separation, facilitates redox reactions and avoids overoxidation.

In summary, this work reported a benchmark performance of methanol conversion by synergy of Pt nanodots and atomic Cu on TiO_2, resulting in the highest H_2 evolution activity of 2383.9 μmol h^{-1} (476.8 mmol g^{-1} h^{-1}), leading to an AQE of 99.2% at 365 nm, together with a high oxidation product formaldehyde synthesis rate of 2259.5 μmol h^{-1} (451.9 mmol g^{-1} h^{-1}) with ca. 98.6% selectivity while the selectivity to CO was very small about 0.06%. Interestingly, the bifunctional Cu controlled the methanol oxidation to form formaldehyde with high selectivity, eliminating CO_2 emission during H_2 production. The characterization results revealed that PtCu-TiO_2 sandwich structure provided a unique electron transfer path where Cu^{2+} acted as an electron bridge to transport the electrons to Pt, thus driving protons reduction, resulting into a very low activation energy of 13.2 kJ/mol. This work explored dual-site single-atom catalysts and synergy between single atoms and nanodots to maximize atom utilization and realize highly selective and

stable production of valuable products (both green H_2 and formaldehyde), opening an important avenue for atomic catalyst design with high efficiency and stability for both reduction and oxidation reactions

Methods

MIL-125 preparation: Typically, a certain amount of terephthalic acid was dissolved in N,N dimethylacetamide (DMF) followed by the introduction of ethanol [47]. Then the required amount of titanium butoxide was added into the above solution dropwise to form a uniform mixture and then transferred to a Teflon-lined stainless-steel autoclave at 130 ^{0}C for 20 hours. After extraction and cooling down, the precipitate was separated, washed by dimethylformamide and methanol using centrifuging at 9000 rpm for 5 min. The solvent was removed by vacuum oven at room temperature to collect MIL-125.

Cu-TiO_2 preparation: MIL-125 was well dispersed in DI water via sonication, followed by the addition of metal-salt with the designed weight ratio (e.g. 0.75 wt% metal on MIL-125). After stirring for 2 hours, the mixture was centrifuged at 9000 rmp for 5 min to obtain metal-MIL-125 (named the ion-coordination method). The TiO_2 with various metal loading (including Fe, Co, Ni, Cu, Ru, Pt) was obtained by calcination of the solid at different temperatures (673-873K) in a muffle oven. Various Cu ratios were loaded on MIL-125 followed by the calcination to obtain Cu-TiO_2, which was later determined by MP-AES as 0.16%, 0.85%, 1.53%, 1.82%, and 2.42%. The $_{1.53\%}$Cu-TiO_2 was named as Cu-TiO_2 in the manuscript and this text unless specifically mentioned. To investigate the condition affect, different calcination temperatures and times were applied for Cu-TiO_2 synthesis. For pure TiO_2, MIL-125 was directly put in a muffle furnace (Carbolite, CWF 1300) for annealing at 500 ^{o}C for 3h.

PtCu-TiO_2 synthesis: Pt was induced on Cu-TiO_2 by an in situ photodeposition method. Typically, 5 mg Cu-TiO_2 and 0.5wt.% of H_2PtCl_6 were dispersed into 40mL 70% methanol aqueous solution. Then the above solution was purged with argon for 20 min to remove oxygen and then sealed for 365 nm LED-induced postdeposition to form PtCu-TiO_2. The preparation of Pt-TiO_2 was the same procedure as the above except using TiO_2 as the substrate. It is worth mentioning that the samples for characterization were obtained by 30 min irradiation using 50mg Cu-TiO_2 to obtain a good signal to noise. From MP-AES, the Pt amount of PtCu-TiO_2 and Pt-TiO_2 was analysed to be 0.25% and 0.17%. The optimal sample $_{1.53\%}Cu_{0.25\%}$Pt-TiO_2 was named as PtCu-TiO_2 while $_{0.17\%}$Pt-TiO_2 was named as Pt-TiO_2 in the manuscript and this text unless specifically stated.

Photocatalysis: The hydrogen generation experiments from the methanol-water mixture were carried out under 365 nm LED irradiation (Perfect Light, Beijing). Usually, 5 mg material and 40 mL 70% methanol solution was added into a 175 mL reactor followed by the illumination. The temperature was kept at room temperature (20 ^{o}C) using a water bath. For the long-term stability test, the sample always remained in the reactor for the test. During the stability test, in run 7, 0.5 mL methanol was added due to the methanol evaporation during argon purging. Then, in run 10, 4 mL 70% methanol was added to maintain the same solution volume. From run 10-14, 0.1 ml methanol was introduced before each reaction due to consumption of methanol. The gases H_2 was analysed by gas chromatography Varian 430-GC with a FID detector. A FID equipped with methanizer in another GC (Varian 450) was used to quantify the concentration of CO_2 and CO. The solution after certain reaction time was sampled for formaldehyde and formic acid detection using ultraviolet-visible diffuse reflectance spectroscopy (an acetylacetone method [48]) and ion chromatography (Eco IC, Column Metrosep A Supp 5), respectively.

Apparent quantum efficiency (AQE) measurement: The apparent quantum efficiency calculation follows $\varphi = \frac{nR}{I}$, where n, R, and I are the involved electrons number, the hydrogen evolution rate and the amount of incident photons, respectively [49]. For all measurements, the irradiation window diameter was 4 cm and the incident light intensity was measured to be 3.5 mW cm^{-2}. The temperature was controlled by a stirring hot plate for measurement at the different reaction temperature. The experiment was carried out a few times under 10 min (600s) light irradiation. The average produced H_2 at 25 °C, 40 °C, 50 °C, 60 °C and 70 °C were 22.6 μmol, 29.5 μmol, 34.4 μmol, 38.8 μmol and 41.6 μmol in the reactor (175 mL), respectively. The AQE at 70 °C was measured under 3.65 mW cm^{-2} light irradiation and the produced H_2 in the reactor was 41.6 μmol. Taking the AQE at 70 °C as an example, the detailed calculation was shown below.

$$I = \frac{E \succ}{hc} \times S = \frac{3.65 \times 10^{-3} \times 600 \times 365 \times 10^{-9}}{6.626 \times 10^{-34} \times 3 \times 10^{8}} \times 3.14 \times 2 \times 2 = 5.05 \times 10^{19}$$

$$\varphi = \frac{nR}{I} = \frac{2 \times 41.6 \times 10^{-6} \times 6.02 \times 10^{23}}{5.05 \times 10^{19}} \times 100\% = 99.2\%$$

Characterization: The powder X-ray diffraction (XRD) patterns of the samples were measured in a Stoe STADI-P instrument (2° to 40°, step 0.5° at 5.0 s/step) using Mo Kα1 (wavelength 0.70930 Å, 50 kV and 30 mA). Ultraviolet-visible diffuse reflectance spectra (UV-vis DRS) were acquired by a Shimadzu UV-Vis 2550 spectrophotometer fitted with an integrating sphere, using Standard barium sulfate as a reference. The morphology and microstructure were investigated by the scanning electron microscope (SEM) (Sirion 200). Transmission electron microscopy images and high-angle annular dark-field (HAADF) STEM were acquired on JEOL 2100F analytical TEM operated at 200 kV. The aberration-corrected high-angle annual dark-filed scanning transmission electron microscopy (AC-HAADF-STEM) analysis was performed on a JEOL JEM-ARM200F equipped with a CEOS probe corrector, with a guaranteed resolution of 0.08 nm. Electron spin resonance (EPR) spectra were collected from MS-5000 spectrometer. The *in situ* XPS data of PtCu-TiO_2 was obtained from PHI 5000 VersaProbe II Scanning XPS Microprobe with six multichannel plates using a 365 nm light source (3000 eV). The XPS data of Cu-TiO_2 obtained various temperatures and PtCu-TiO_2 were recorded from a Kratos Axis SUPRA XPS fitted with a monochromatic Al kα X-ray source (1486.7 eV), a spherical sector analyser and three multichannel resistive plates, 128 channel delay line detectors. Survey scans were recorded at a pass energy of 160 eV, and high-resolution scans recorded at a pass energy of 20 eV. All data was collected at 150W and a spot size of 700 x 300 μm. Data were analysed using CasaXPS and the spectra were calibrated with C1s peak at 284.8 eV. The XPS spectra for Cu-TiO_2 before and after the reaction were collected from a Thermo Scientific NEXSA XPS system with an Al Kα X-ray source. Raman spectra were measured using a Renishaw inVia Raman microscope. The lifetime of the photogenerated charge carriers was acquired by a time-resolved fluorescence decay spectroscopy (FL-1039A/40A) using 320 nm and 450 nm as the excitation and emission wavelengths. The determination of metal amount was performed by microwave plasma atomic emission spectrometry (MP-AES Agilent 4200). Photo-electrochemical test was carried out by a three-electrode electrolytic cell, where the FTO electrode coated with the photocatalyst worked as the working electrode, the platinum plate acted as the counter electrode, and the Ag/AgCl electrode acted as the reference electrode. A 150 W xenon lamp was used as the arc light source and 70 mL of 0.5 M Na_2SO_4 solution with 10% methanol served as the electrolyte. In detail, the photocurrent test was performed using a

potentiostatic technique with a switching period of 2 s. The scan rate for the cycling voltammetry was 2mV/s. The electrochemical impedance spectra were collected using the same three-electrode system with the following parameters: at 0 V vs. Ag/AgCl and amplitude 10 mV. The X-ray absorption spectra including X-ray absorption near-edge structure (XANES) and extended X-ray absorption fine structure (EXAFS) at the K-edge of Cu and L_{III}-edge of Pt of the samples, were collected at the BL 14W1 of Shanghai Synchrotron Radiation Facility (SSRF), China. The Cu and Pt foil was employed to calibrate the energy. The spectra were collected at fluorescence mode at room temperature. The Athena software package was used to analyse the data. The details Density Functional Theory (DFT) calculation was shown in the supporting information.

Steady-state UV−vis−NIR diffuse-reflectance spectroscopy: The signal detection was performed by a Cary 5000 UV-vis-NIR spectrometer, which was equipped with a Praying Mantis accessory. A filter (>395 nm) was installed before the sample beam detector, avoiding the reflection of excitation light caused by the samples. The reactor was equipped with three quartz windows with 2mm thickness (Crystran, QPZ15-2). One was for excitation light passing and the other two were for the light transmission. In the system, the 300 W Xe lamp (Newport, model 67005) with a filter (325-385 nm, Thorlabs, FGUV UG1) and a 365 nm bandpass filter (Comar) served as the irradiation source. Argon, dry air and methanol acted as an insert reference, electron consumer and hole scavengers, respectively. For all measurements, the reactor was sealed for measurements after 30 min gas feeding via a flow rate of 100 mL/min, achieving an adsorption/desorption balance.

***In situ* NEXAFS measurements:** *In situ* NEXAFS measurements in the total electron yield mode were performed at the Photoemission Endstation (BL10B) in the National Synchrotron Radiation Laboratory (NSRL) in Hefei, China. This beamline is connected to a bending magnet and equipped with three gratings that cover photon energies from 100 to 1000 eV with a typical photon flux of 1 × 1010 photons/s and a resolution (E/ΔE) better than 1000 at 244 eV. Spectra were collected at energies from 455 to 477 eV for Ti L-edge NEXAFS spectra and 515 to 575 eV for O K-edge NEXAFS spectra in a 0.2 eV energy step. UV light illumination was accomplished using a 320 nm LED lamp placed at 15 cm in front of the sample. The NEXAFS raw data were processed as the following: firstly, the photon energy was calibrated from the 4f spectral peak of a freshly sputtered gold wafer, then a line was subtracted to set the pre-edge as zero, and finally the spectrum was normalized to yield an edge-jump to one.

References

1. Palo, D. R., Dagle, R. A. & Holladay, J. D. Methanol steam reforming for hydrogen production. *Chem. Rev.* **107**, 3992–4021 (2007).
2. Turner, J. A. Sustainable Hydrogen Production. *Science (80-.).* **305**, 972–974 (2004).
3. Nielsen, M. *et al.* Low-temperature aqueous-phase methanol dehydrogenation to hydrogen and carbon dioxide. *Nature* **495**, 85–89 (2013).
4. Cortright, R. D., Davda, R. R. & Dumesic, J. A. Hydrogen from catalytic reforming of biomass-derived hydrocarbons in liquid water. *Nature* **418**, 289–292 (2002).
5. Olah, G. A. Beyond oil and gas: The methanol economy. *Angew. Chemie - Int. Ed.* **44**, 2636–2639 (2005).

6. Palo, D. R. Methanol steam reforming for hydrogen production. *Chem. Rev.* **107**, 3992–4021 (2007).

7. Lin, L. *et al.* Low-Temperature hydrogen production from water and methanol using Pt/α-MoC catalysts. *Nature* **544**, 80–83 (2017).

8. Varas-Concha, F., Guzmán, D., Isaacs, M. & Sáez-Navarrete, C. Operational conditions affecting formaldehyde and formic acid formation as by-products of hydrogen production via photo-reforming of methanol using nanoparticles of TiO_2. *Energy Technol.* **6**, 1871–1884 (2018).

9. Solt, P. *et al.* Technological performance of formaldehyde-free adhesive alternatives for particleboard industry. *Int. J. Adhes. Adhes.* **94**, 99–131 (2019).

10. Ruf, S., May, A. & Emig, G. Anhydrous formaldehyde by sodium catalysis. *Appl. Catal. A Gen.* **213**, 203–215 (2001).

11. Bahmanpour, A. M., Hoadley, A. & Tanksale, A. Critical review and exergy analysis of formaldehyde production processes. *Rev. Chem. Eng.* **30**, 583–604 (2014).

12. Pernicone, N. Deactivation of Fe-Mo oxide catalyst in industrial plant and simulation tests on laboratory scale. *Catal. Today* **11**, 85–91 (1991).

13. Christopher, P., Xin, H. & Linic, S. Visible-light-enhanced catalytic oxidation reactions on plasmonic silver nanostructures. *Nat. Chem.* **3**, 467–472 (2011).

14. Wang, Q. *et al.* Scalable water splitting on particulate photocatalyst sheets with a solar-to-hydrogen energy conversion efficiency exceeding 1%. *Nat. Mater.* **15**, 611–615 (2016).

15. Fox, Marye Anne, Ma. T. D. Heterogeneous photocatalysis. *ChemEngineering* **93**, 341–357 (1993).

16. Lee, B. H. *et al.* Reversible and cooperative photoactivation of single-atom Cu/TiO_2 photocatalysts. *Nat. Mater.* **18**, 620–626 (2019).

17. Zhang, C. & Tour, J. M. Atomic approaches towards stability. *Nat. Catal.* **1**, 900–902 (2018).

18. Fei, H. *et al.* Single atom electrocatalysts supported on graphene or graphene-like carbons. *Chem. Soc. Rev.* **48**, 5207–5241 (2019).

19. Zhang, Y. *et al.* Single-atom Cu anchored catalysts for photocatalytic renewable H_2 production with a quantum efficiency of 56%. *Nat. Commun.* **13**, (2022).

20. Liu, J. *et al.* Enhancement of photochemical hydrogen evolution over Pt-loaded hierarchical titania photonic crystal. *Energy Environ. Sci.* **3**, 1503–1506 (2010).

21. Yu, J., Hai, Y. & Cheng, B. Enhanced photocatalytic H_2-production activity of TiO_2 by Ni(OH)2 cluster modification. *J. Phys. Chem. C* **115**, 4953–4958 (2011).

22. Xiao, S. *et al.* Copper nanowires: a substitute for noble metals to enhance photocatalytic H2 generation. *Nano Lett.* **15**, 4853–4858 (2015).

23. Ou, G. *et al.* Tuning defects in oxides at room temperature by lithium reduction. *Nat. Commun.* **9**, 1–9 (2018).

24. Chiarello, G. L., Aguirre, M. H. & Selli, E. Hydrogen production by photocatalytic steam

reforming of methanol on noble metal-modified TiO_2. *J. Catal.* **273**, 182–190 (2010).

25. Jin, J. *et al.* Anchoring ultrafine metallic and oxidized Pt nanoclusters on yolk-shell TiO_2 for unprecedentedly high photocatalytic hydrogen production. *Nano Energy* **38**, 118–126 (2017).

26. Wang, H. Titanosilicate zeolite supported Pt nanoparticles with electronic metal-support interactions for efficient methanol steam reforming. *Catal. Today* **382**, 42–47 (2021).

27. Sun, Z., Fang, S., Lin, Y. & Hu, Y. H. Photo-assisted methanol steam reforming on solid solution of Cu-Zn-Ti oxide. *Chem. Eng. J.* **375**, 121909 (2019).

28. Uchihara, T., Matsumura, M., Yamamoto, A. & Tsubomura, H. Effect of platinum loading on the photocatalytic activity and luminescence of cadmium sulfide powder. *J. Phys. Chem.* **93**, 5870–5874 (1989).

29. Shiraishi, Y., Sakamoto, H., Sugano, Y., Ichikawa, S. & Hirai, T. Pt-Cu bimetallic alloy nanoparticles supported on anatase TiO2: Highly active catalysts for aerobic oxidation driven by visible light. *ACS Nano* **7**, 9287–9297 (2013).

30. Luca, G., Ferri, D. & Selli, E. Effect of the CH_3OH/H_2O ratio on the mechanism of the gas-phase photocatalytic reforming of methanol on noble metal-modified TiO_2. *J. Catal.* **280**, 168–177 (2011).

31. Chiarello, G. L., Aguirre, M. H. & Selli, E. Hydrogen production by photocatalytic steam reforming of methanol on noble metal-modified TiO_2. *J. Catal.* **273**, 182–190 (2010).

32. Xie, S. *et al.* Visible light-driven C-H activation and C-C coupling of methanol into ethylene glycol. *Nat. Commun.* **9**, 1–7 (2018).

33. Mi, Q., Coridan, R. H., Brunschwig, B. S., Gray, H. B. & Lewis, N. S. Photoelectrochemical oxidation of anions by WO_3 in aqueous and nonaqueous electrolytes. *Energy Environ. Sci.* **6**, 2646–2653 (2013).

34. Wang, Z. Overall water splitting by Ta_3N_5 nanorod single crystals grown on the edges of KTaO3 particles. *Nat. Catal.* **1**, 756–763 (2018).

35. Maeda, K. *et al.* GaN:ZnO solid solution as a photocatalyst for visible-light-driven overall water splitting. *J. Am. Chem. Soc.* **127**, 8286–8287 (2005).

36. Brack, P., Dann, S. E., Wijayantha, K. G. U., Adcock, P. & Foster, S. An old solution to a new problem? Hydrogen generation by the reaction of ferrosilicon with aqueous sodium hydroxide solutions. *Energy Sci. Eng.* **3**, 535–540 (2015).

37. Byrne, C. *et al.* Effect of Cu doping on the anatase-to-rutile phase transition in TiO_2 photocatalysts: Theory and experiments. *Appl. Catal. B Environ.* **246**, 266–276 (2019).

38. Zhang, Y., Harris, C. X., Wallenmeyer, P., Murowchick, J. & Chen, X. Asymmetric lattice vibrational characteristics of rutile TiO_2 as revealed by laser power dependent raman spectroscopy. *J. Phys. Chem. C* **117**, 24015–24022 (2013).

39. Espinós, J. P. *et al.* Interface effects for Cu, CuO, and Cu_2O deposited on SiO_2 and ZrO_2. XPS determination of the valence state of copper in Cu/SiO_2 and Cu/ZrO_2 catalysts. *J. Phys. Chem. B* **106**, 6921–6929 (2002).

40. Raman, R. K. *et al.* Tailoring a Pt-Ru catalyst for enhanced methanol electro-oxidation. *J.*

Power Sources **157**, 45–55 (2006).

41. Briggs, D. X-ray photoelectron spectroscopy (XPS). *Handb. Adhes. Second Ed.* 621–622 (2005) doi:10.1002/0470014229.ch22.
42. Ardelean, I., Peteanu, M., Ciceo-Lucacel, R. & Bratu, I. Structural investigation of CuO containing strontium-borate glasses by means of EPR and IR spectrometry. *J. Mater. Sci. Mater. Electron.* **11**, 11–16 (2000).
43. Miao, T. J. *et al.* In situ investigation of charge performance in anatase TiO_2 powder for methane conversion by Vis-NIR dpectroscopy. *ACS Catal.* **11**, 8226–8238 (2021).
44. Berera, R., van Grondelle, R. & Kennis, J. T. M. Ultrafast transient absorption spectroscopy: Principles and application to photosynthetic systems. *Photosynth. Res.* **101**, 105–118 (2009).
45. Tang, J., Durrant, J. R. & Klug, D. R. Mechanism of photocatalytic water splitting in TiO_2. Reaction of water with photoholes, importance of charge carrier dynamics, and evidence for four-hole chemistry. *J. Am. Chem. Soc.* **130**, 13885–13891 (2008).
46. Holzl, J. & Shulte F.K. Work Functions of Metals. *Solid Surface Physics* 1–150 (1979).
47. Dan-Hardi, M. *et al.* A New Photoactive Crystalline Highly Porous Titanium(IV) Dicarboxylate. *J. Am. Chem. Soc.* **131**, 10857–10859 (2009).
48. S. Fregert. A simple method for the detection of fromaldehyde. *Contact Dermatitis* **10**, 132–134 (1984).
49. Hisatomi, T., Takanabe, K. & Domen, K. Photocatalytic water-splitting reaction from catalytic and kinetic perspectives. *Catal. Letters* **145**, 95–108 (2015).

Data and materials availability: All data are available in the manuscript or the supplementary information.

Acknowledgments: All authors thank to Photoemission Endstation (BL10B) in the National Synchrotron Radiation Laboratory (NSRL) in Hefei. H. Wang, X. Li, T. Miao,L.Xiong and J. Tang are thankful for UK EPSRC (EP/S018204/2), Leverhulme Trust (RPG-2017-122), Royal Society Newton Advanced Fellowship grant (NAF\R1\191163), and Royal Society Leverhulme Trust Senior Research Fellowship (SRF\R1\21000153).

Author contributions: J. Tang designed and supervised the entire project and oversaw all discussions. H. Wang conducted the catalysts preparation, sample characterisations, activity tests. H. Qi carried out the EXAFS and fitted the data. X. Li contributed to the EPR discussion. T. Miao helped to collect data and discussion of UV-Vis-NIR diffuse-reflectance spectra. S. Jia carried out DTF calculation and X. Zhang supervised the process. X. Sun collected Ti, O EXAFS data and W. Huang supervised the process. L. Xiong performed AC-HAADF-STEM. S. Wang collected all TEM data. X. Liu, A. Wang and T. Zhang supervised the EXAFS data collection and fitting. The manuscript was written through collective contributions from all authors. All authors approved the final version of the manuscript.

Competing interests: The authors declare no competing interests.